

Discretely Tunable (2594, 2629, 2670 nm) GaSb/Si₃N₄ Hybrid Laser for Multiwavelength Spectroscopy

Samu-Pekka Ojanen,* Jukka Viheriälä, Nouman Zia, Eero Koivusalo, Joonas Hilska, Heidi Tuorila, and Mircea Guina

A discrete, tunable photonic integrated laser is showcased for multiwavelength spectroscopy of CO₂, H₂S, and H₂O. The laser combines an AlGaInAsSb/GaSb type-I quantum well-reflective semiconductor optical amplifier with a Si₃N₄ photonic integrated circuit (PIC). Operating at room temperature, the laser emits at 2670.42, 2629.12, and 2594.27 nm, with mW-level average powers. The PIC employs a novel approach for achieving switching between three distinct emission wavelengths by using two cascaded tunable Mach–Zehnder interferometers (MZIs) that are connected to three spiral-shaped narrow-band distributed Bragg reflectors (DBRs). Phase tuning the arms of the MZIs allows the laser emission wavelength to be switched between the DBRs, while the DBRs themselves offer fine-tuning of the emission wavelength. This design enables a simpler tuning mechanism with fewer control variables compared to hybrid PIC-based lasers using Vernier architectures or a combination of multiple semiconductor amplifiers. Low-loss and broadband MZIs are achieved by employing two interconnected directional couplers, which utilize asymmetric waveguides in the coupling region to effectively control the phase. Besides achieving state-of-the-art performance for Si₃N₄-based integrated lasers at 2.6 μm wavelength region, the demonstrated performance of passive components, including MZIs and spiral DBRs, opens new possibilities for mid-infrared PIC technology.

includes absorption bands for several important industrial and environmental gases, including H₂S, C₂H₄, CH₄, CO, CO₂, and N₂O,^[3] as well as important biomarkers such as lactate, urea, and glucose.^[4,5] Selective and sensitive detection of these gases and biomarkers is essential for a range of applications, from environmental monitoring^[6] to disease diagnosis and prevention.^[7]

Many conventional light sources, such as solid-state lasers, monolithic laser diodes, and external cavity laser diodes, are typically bulky, expensive, and lack versatility and scalability. In contrast, hybrid integrated light sources, which combine III/V semiconductor optical amplifiers (SOAs) with tunable photonic integrated circuits (PICs), offer significant advantages, including versatility, miniaturization, efficiency, and volume scalability. These sources deliver sufficient power with high spectral purity and broad tunability.^[8,9]

The integration of GaSb-based type-I quantum well (QW) SOAs with PICs presents a unique platform for


developing hybrid integrated light sources in the 2–4 μm wavelength band.^[10–12] This integration enables the design of compact and efficient multiwavelength sensors. Furthermore, the combination of GaSb-based SOAs and low-loss PICs facilitates high-output power generation. This characteristic proves particularly advantageous in sensing applications, as it reduces the signal-to-noise ratio (SNR), leading to improved sensitivity and accurate measurement of smaller gas concentrations. Moreover, GaSb-based SOAs offer broad tunability, allowing access to a wider range of absorption lines.^[13,14] This capability enables the measurement of multiple gases and enhances specificity and selectivity in distinguishing between different gases.

Sensing applications often require the ability to access multiple absorption features to detect different analytes, and to improve sensitivity and selectivity for accurate and reliable measurements. Therefore, it is crucial for the hybrid light source to cover a wide range of wavelengths. This can be achieved with a broadly tunable laser, which can be adjusted to any wavelength within the gain bandwidth of the SOA. Alternatively, a multiwavelength laser (MWL) can emit and be tuned around specific wavelengths within the SOA's gain bandwidth.

1. Introduction

The mid-infrared wavelength region has emerged as an important spectral range for both gas sensing and biosensing applications.^[1,2] In particular, the 2–4 μm wavelength region

S.-P. Ojanen, J. Viheriälä, N. Zia, E. Koivusalo, J. Hilska, H. Tuorila, M. Guina
Optoelectronics Research Centre
Photonics Laboratory
Physics Unit
Faculty of Engineering and Natural Sciences
Tampere University
Korkeakoulunkatu 3, Tampere 33720, Finland
E-mail: samu-pekka.ojanen@tuni.fi

 The ORCID identification number(s) for the author(s) of this article can be found under <https://doi.org/10.1002/lpor.202300492>

© 2023 The Authors. Laser & Photonics Reviews published by Wiley-VCH GmbH. This is an open access article under the terms of the Creative Commons Attribution License, which permits use, distribution and reproduction in any medium, provided the original work is properly cited.

DOI: 10.1002/lpor.202300492

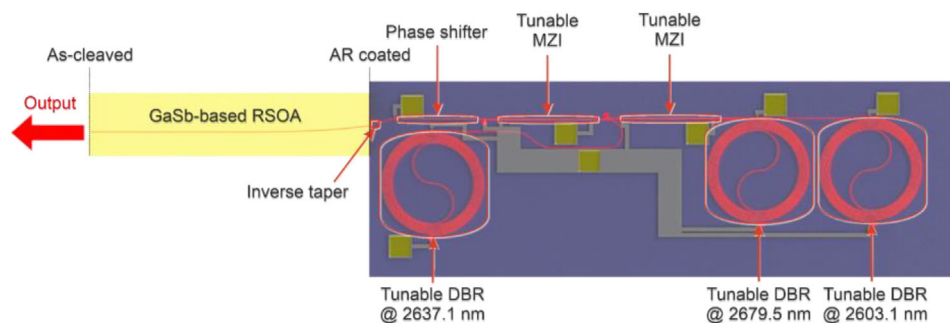


Figure 1. Schematic of the GaSb/Si₃N₄ hybrid MWL demonstrated in this work.

Although there is growing interest in developing hybrid tunable lasers in the 2–3 μm range, there have been few reports thus far, mostly limited to implementations based on the Vernier effect,^[13–16] utilizing two tunable ring resonators. While the Vernier laser offers an excellent tuning range and spectral purity, achieving a precise operation point poses challenges due to the need to tune three control variables: the resonance wavelengths of the two ring resonators, and the phase of the laser cavity.

In the case of MWLs, an array of distributed feedback (DFB) lasers has been demonstrated around the 2.3 μm , utilizing silicon gratings beneath heterogeneously integrated SOAs.^[17] Such a DFB laser array requires less precise control over the laser cavity and has simpler tuning requirements compared to a Vernier laser. However, each wavelength in this type of laser requires its own SOA, which increases the footprint, the cost, and the complexity compared to a Vernier laser.

On the other hand, in the 1.55 μm wavelength region, a MWL based on an arrayed waveguide grating (AWG) with a heterogeneously integrated SOA has been demonstrated.^[18] This configuration allows for simultaneous emission at four distinct wavelengths with high stability and fewer control parameters compared to the Vernier laser. However, in this case, wavelength tuning is achieved by adjusting the chip temperature, limiting the tuning speed of the laser. Additionally, the tuning range is constrained by the linewidth of the AWG channels (<3 nm).

We propose a novel MWL architecture that combines a single GaSb-based reflective SOA (RSOA) with a Si₃N₄ PIC. This architecture incorporates a unique laser emission switching capability through two thermally tunable Mach–Zehnder interferometers (MZIs) that are coupled to three thermally tunable narrow-band distributed Bragg reflectors (DBRs). By adjusting the MZI arms, the laser emission wavelength can be switched between the DBRs. Additionally, fine-tuning of the emission wavelength is possible by tuning the DBRs. A phase shifter is also integrated to allow phase-matching of the RSOA and the PIC to achieve maximum power and spectral purity. In a Vernier laser, wavelength tuning requires tuning of at least two ring resonators and the phase of the cavity, leading to a minimum 3D tuning map. In contrast, in our approach, wavelength tuning requires tuning of a single DBR and the cavity phase, leading to a simpler 2D tuning map. This leads to faster laser calibration and simpler tuning mechanism.

Moreover, unlike previous MWL approaches that require a separate SOA for each target wavelength, our design achieves multiwavelength emission by utilizing only one SOA that operates

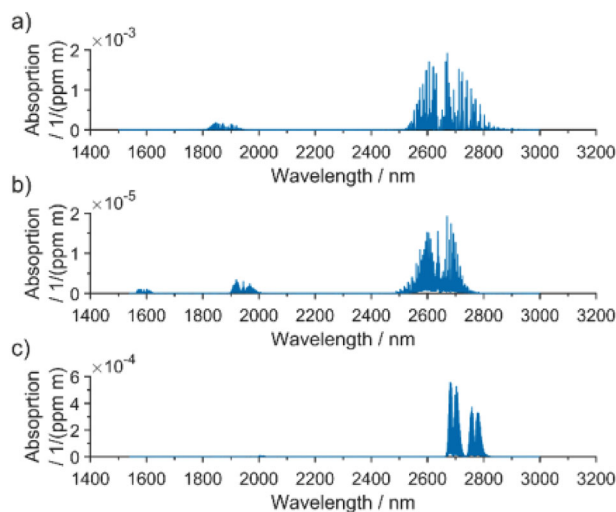


Figure 2. Absorption as a function of wavelength for a) H₂O, b) H₂S, and c) CO₂.^[3]

within its gain bandwidth. Furthermore, in the context of sensing systems, it is common for target wavelengths to not align precisely with the gain bandwidth of a single SOA. In such cases, our approach offers a distinct advantage by minimizing the number of required SOAs. By capitalizing on the ability of a single SOA to accommodate multiple target wavelengths falling within its gain bandwidth, the approach is effective in reducing the footprint, complexity, and cost of the sensing system.

Figure 1 shows a schematic of the tunable GaSb/Si₃N₄ hybrid MWL proposed and demonstrated in this work. The RSOA utilized in the hybrid MWL employs a “J-shaped” waveguide, where the front facet has a bend waveguide with a 7° output angle to suppress reflections, and the rear facet has a straight waveguide with an as-cleaved facet to provide $\approx 30\%$ reflectance. The PIC incorporates low-loss 800-nm-thick Si₃N₄ waveguides fabricated utilizing LIGENTEC’s open-access foundry services, which we have previously demonstrated to be capable of producing high-performance hybrid lasers within the 2.0–2.7 μm wavelength range.^[13,14] The facets at the coupling interface were anti-reflectance (AR) coated to minimize parasitic reflections, and to maximize transmission.

The hybrid MWL was designed to target H₂O, H₂S, and CO₂ absorption lines in the 2.6–2.7 μm wavelength region, where these gases exhibit strong fingerprints (see **Figure 2**). To be more

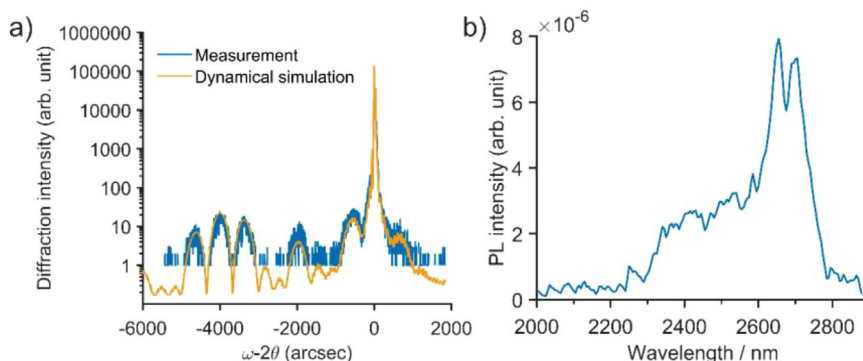


Figure 3. a) HR-XRD measurement centered around the GaSb(004) reflex from the epitaxial structure together with a dynamical simulation fitted to the data, and b) the PL signal as a function of wavelength for the AlGaInAsSb/GaSb type-I QW epitaxial structure utilized in this work.

precise, the nominal DBR resonance wavelengths were designed for emission at 2605.6, 2639.6, and 2682.0 nm, respectively. To accommodate the wavelength variation in the multi-project wafer (MPW) process, the DBR resonances were designed to be 2.5 nm shorter than the absorption lines, while resistive heaters were implemented to thermally tune the DBR resonances to align with the absorption lines. The target DBR resonances are shown in Figure 1.

2. Characterization of AlGaInAsSb/GaSb Epimaterial and RSOAs

To generate light in the 2.6–2.7 μm wavelength region, an AlGaInAsSb/GaSb type-I QW structure was utilized. The epitaxial structure consisted of two compressively strained $\text{Ga}_{0.50}\text{In}_{0.50}\text{As}_{0.20}\text{Sb}_{0.80}$ QWs with 1.7% strain, and an $\text{Al}_{0.30}\text{Ga}_{0.70}\text{As}_{0.02}\text{Sb}_{0.98}$ barrier in between. The QW layers were sandwiched between two 270-nm-thick $\text{Al}_{0.30}\text{Ga}_{0.70}\text{As}_{0.02}\text{Sb}_{0.98}$ waveguide layers. The waveguide layers were placed between 2- μm -thick $\text{Al}_{0.60}\text{Ga}_{0.40}\text{As}_{0.05}\text{Sb}_{0.95}$ p- and n-doped cladding layers. The doping levels in the inner 500 nm part of the cladding were graded close to the waveguide layers to minimize free carrier absorption near the active region. The alloy compositions and QW-strain given were determined from high-resolution X-ray diffraction measurements (HR-XRD) and corresponding simulations based on the dynamical diffraction theory.^[19] This is shown in Figure 3a. In the simulations, group III alloy-compositions were determined from constituent binary material (e.g., GaAs, AlAs) growth rates given their unity sticking coefficients. The doping levels in the inner 500 nm of cladding were graded close to the waveguide layers to minimize free carrier absorption near the active region.

The photoluminescence (PL) spectrum of the AlGaInAsSb/GaSb type-I QW epitaxial structure was measured in the 2.0–2.9 μm wavelength region. Figure 3b shows the intensity of the PL signal as a function of wavelength. Based on the data, the gain covers the 2.60–2.75 μm wavelength region, albeit with some uncertainty due to atmospheric absorption, which causes distortion in the data.

A 2000- μm -long and 550- μm -wide RSOA chip, consisting of a single-mode 5 μm -wide ridge waveguide (RWG) etched up to the p-cladding layer, was manufactured from the epitaxial structure

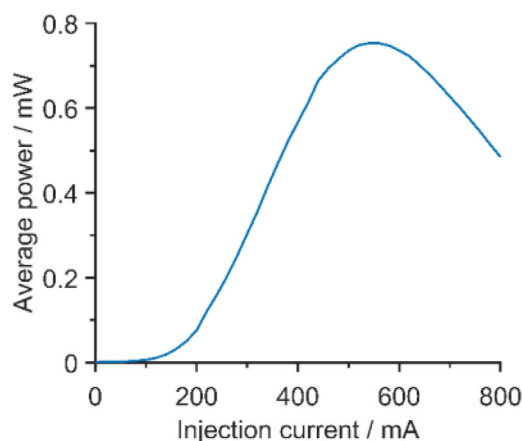


Figure 4. The ASE average power of the RSOA as a function of injection current at 23 $^{\circ}\text{C}$.

to provide gain and feedback in the hybrid laser cavity. The RSOA was mounted p-side down with indium on an AlN submount to achieve efficient heat dissipation from the active region. The amplified spontaneous emission (ASE) output power from the front facet of the RSOA was measured with an integrating sphere and a photodetector. Pulsed current with 100 kHz frequency and 10% duty cycle was injected to the RSOA to minimize heating effects. Figure 4 shows the ASE average power as a function of injection current. The RSOA reaches a maximum ASE average power of 0.75 mW at an injection current of 540 mA.

3. Design and Simulation of Si_3N_4 Building Blocks

To achieve single-mode propagation within the Si_3N_4 waveguide, a width of 1.65 μm was selected.^[14] This leads to a propagation loss of 0.67 dB cm^{-1} , and a bend loss of 0.017 dB for a 50 μm bend radius.^[14] To couple the RSOA efficiently to the Si_3N_4 PIC, a 50- μm -long tapered waveguide, where the waveguide width tapers down to 0.4 μm width was used at the coupling interface. This leads to a measured coupling loss of ≈ 3 dB.^[14] The inverse taper was placed at a 17 $^{\circ}$ angle to match the output angle of the RSOA.

To enable switching between different DBRs in the Si_3N_4 circuit, two thermally tunable MZIs were employed in a cascaded

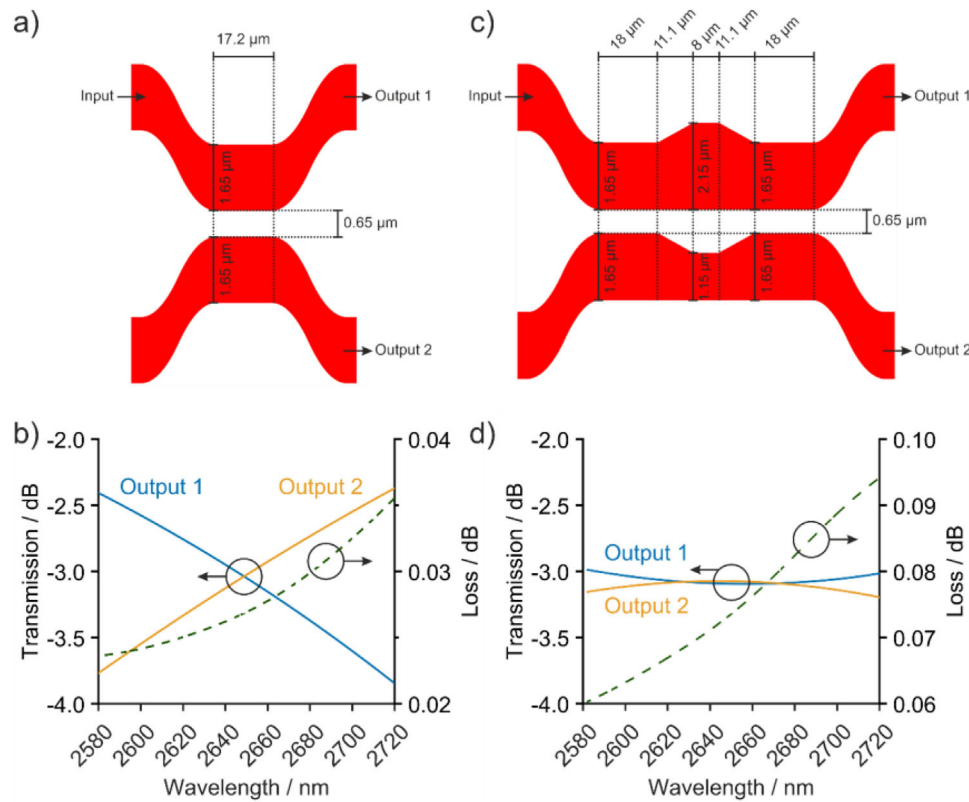


Figure 5. a) Schematic of the 50:50 DC, b) the transmission of the two outputs, and the loss of the 50:50 DC as a function of wavelength, c) schematic of the 50:50 PC-DC, and d) the transmission of the two outputs, and the loss of the 50:50 PC-DC as a function of wavelength.

configuration. These MZIs consisted of two 50:50 waveguide couplers interconnected. In the hybrid MWL, the minimum and maximum wavelengths are separated by 80 nm. Therefore, selecting the appropriate coupler type is crucial to ensure a wide bandwidth and minimal losses for maintaining high laser performance. Typically, there are two common types of waveguide couplers: directional couplers (DCs) and multimode interference (MMI) couplers. DCs exhibit low loss but have limited bandwidth due to significant variations in coupling ratio with wavelength.^[20] On the other hand, MMI couplers offer broadband operation but often suffer from higher losses.^[21] To address these challenges, a broadband phase-controlled DC (PC-DC) was designed, incorporating asymmetric waveguides to control the phase and achieve both broadband and low-loss operation.^[20]

Simulations were performed on two designs: a conventional 50:50 DC, and a 50:50 PC-DC. The design of the directional couplers was optimized utilizing Ansys Lumerical FDTD by varying the geometry and calculating the bandwidth, transmission, and loss to find the optimum geometry. **Figure 5a** shows a schematic of the conventional 50:50 DC. The design consists of two waveguide arms, which are brought together and then separated utilizing “S-shaped” bends with a bend radius of 66 μm , to minimize bend losses. To achieve 50:50 split ratio at 2.65 μm wavelength, an optimum coupling length of 17.2 μm , and an optimum coupling gap of 0.65 μm were found through simulation. **Figure 5b** shows the simulated transmission through the two output waveguides of the 50:50 DC, as well as the simulated loss of the 50:50 DC as a function of wavelength. While the loss is very low (≈ 0.03 dB),

there is a significant variance (≈ 1 dB) in the split ratio in the 2.6–2.7 μm wavelength region. **Figure 5c** shows a schematic of the 50:50 PC-DC. The 50:50 PC-DC coupling region consisted of two 18- μm -long symmetric couplers with an 8- μm -long asymmetric phase-control section in between, connected by 11.1- μm -long tapered waveguides. The coupling gap was set to 0.65 μm . **Figure 5d** shows the simulated transmission to the two output waveguides of the 50:50 PC-DC, as well as the simulated loss of the 50:50 PC-DC as a function of wavelength. While the loss of the coupler is slightly larger (≈ 0.08 dB) compared to the 50:50 DC, the variance in the split ratio in the 2.6–2.7 μm wavelength region is significantly smaller (≈ 0.05 dB), which makes it optimal to be used in the MZIs of the hybrid MWL.

To measure the loss of the PC-DC, a series of 20 PC-DCs were manufactured, and the transmission of this circuit was compared to a straight waveguide, utilizing a Norcada 2.68 μm DFB laser. An estimated loss of ≈ 0.2 dB at 2.68 μm was obtained from the measurement. The split ratio of the PC-DC could not be measured as the output waveguides were placed too close to each other at the PIC facet to be able to distinguish them from each other.

To achieve tunability for the MZI, a heater was placed above both waveguide arms, allowing the tuning of transmission to the two MZI output waveguides by heating up the waveguide to change its refractive index through the thermo-optic effect. Changing the refractive index of one of the waveguides changes the phase of the propagating light, allowing to change the phase difference between the fields propagating in the two MZI arms.

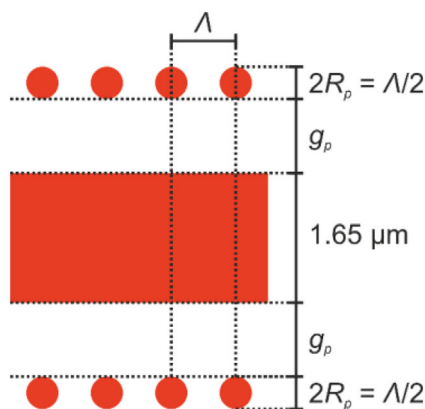


Figure 6. A schematic of the DBR with circular posts with a DBR period Λ , a gap g_p between the waveguide and the post, and radius of the post $R_p = \Lambda/4$.

With sufficient phase shift it is possible to switch the transmission between MZI outputs 1 and 2. The length of the heater was set as $650 \mu\text{m}$ to allow 2π tuning without damaging the heater.^[14] Based on Ansys Lumerical FDE simulations, the heaters do not cause any additional losses. The $650\text{-}\mu\text{m}$ -long waveguides in the MZI arms lead to an additional 0.04 dB insertion loss,^[14] meaning the total loss of the MZI is $\approx 0.44 \text{ dB}$.

Three first-order DBRs were designed, with resonance wavelengths of 2603.1 , 2637.1 , and 2679.5 nm . To achieve sufficiently narrow DBR reflectance band, a very weak change in index in the order of 1×10^{-3} is required. This is very difficult to achieve with a corrugated DBR, as it requires varying the width in the order of $5\text{--}10 \text{ nm}$, which is very close to the resolution limit of the MPW process. To circumvent this problem, periodic index change was achieved by placing circular posts periodically next to the waveguide.^[22] A schematic of the circular post DBR is shown in **Figure 6**. The DBR resonance λ_{DBR} is determined by the DBR period Λ , and the average effective index of the DBR. The diameter of the circular posts $2R_p$ was set to be equal to half of Λ . By changing the gap g_p between the waveguide and the circular posts, the index change, and thus the DBR linewidth $\Delta\lambda_{\text{DBR}}$ can be adjusted.

To achieve single-mode lasing at a single wavelength, the maximum $\Delta\lambda_{\text{DBR}}$ was set at 0.4 nm . A series of simulations were performed with Ansys Lumerical EME to find the values for g_p and Λ to match the target resonance wavelengths, and to keep $\Delta\lambda_{\text{DBR}}$ below 0.4 nm . In addition, the magnitude of the DBR reflectance and $\Delta\lambda_{\text{DBR}}$ was simulated as a function of length of the DBR L_{DBR} , and the result is shown in **Figure 7** for a DBR with Λ and g_p of 832.67 and 944 nm , respectively. To ensure $\Delta\lambda_{\text{DBR}} < 0.4 \text{ nm}$, L_{DBR} must be $>9 \text{ mm}$. To maximize reflectance, L_{DBR} of 12 mm was chosen, leading to a reflectance of ≈ 0.87 and $\Delta\lambda_{\text{DBR}}$ of $\approx 0.36 \text{ nm}$ in the case of the DBR shown in **Figure 7**. **Table 1** shows a summary of the simulated Λ , λ_{DBR} , g_p , and $\Delta\lambda_{\text{DBR}}$ values for all the three DBRs.

To manufacture a grating with L_{DBR} of 12 mm , straight DBR gratings cannot be used, since the target size of the PICs is in the mm-range. To achieve long DBRs, a spiral-shaped DBR geometry was utilized with the circular Si_3N_4 posts placed next to the bent Si_3N_4 waveguide.^[22] As the waveguide bend radius increases, it

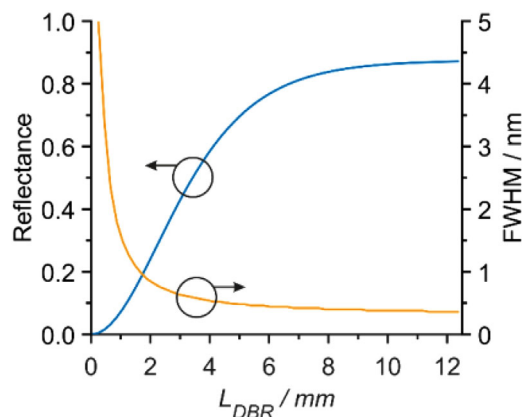


Figure 7. Reflectance and FWHM as a function of length L_{DBR} for a DBR with period Λ and gap g_p of 832.67 and 944 nm , respectively.

Table 1. Target gas, period Λ , simulated resonance wavelength λ_g , gap g_p , simulated linewidth $\Delta\lambda_g$ for the three DBRs used in this work.

Target gas	Λ [nm]	λ_g [nm]	g_p [nm]	$\Delta\lambda_g$ [nm]
H_2O	793.81	2603.07	947	0.30
H_2S	807.07	2637.10	948	0.31
CO_2	832.67	2679.48	944	0.36

influences the mode shape, which changes the effective index of the waveguide mode, shifting λ_{DBR} . This could be circumvented by using a different Λ or g_p for each bend radius. However, to simplify the design, all DBR parameters were kept constant, and a sufficiently large minimum bend radius was chosen to keep the shift in λ_{DBR} as small as possible. A series of simulations were performed with Ansys Lumerical EME, using the design parameters of the DBR targeting CO_2 , with different bend radii to see how λ_{DBR} shifts as the bend radius increases. **Figure 8a** shows the simulated shift in resonance as a function of bend radius. Based on the simulation result, a round spiral-shaped DBR was designed, where the minimum bend radius for the outer waveguide bends was set to $290 \mu\text{m}$, leading to a negligible resonance shift of $<0.034 \text{ nm}$ in the outer waveguides, while the inner S-bend has a bend radius of $145 \mu\text{m}$, leading to a resonance shift of $\approx 0.14 \text{ nm}$, which, while larger than the resonance shift in the outer bends, still stays within the linewidth $\Delta\lambda_{\text{DBR}}$ of the DBR. The gap between adjacent waveguides in the spiral was set to $8.35 \mu\text{m}$, which is sufficiently large to prevent evanescent coupling between waveguides. A schematic of the spiral-shaped DBR geometry used in this work is shown in **Figure 8b**.

To be able to achieve laser emission at the target gas absorption lines, the DBR's reflection should be tunable. This was achieved by placing a $2.5\text{-}\mu\text{m}$ -wide heater layer above the Si_3N_4 waveguide, making it possible to tune λ_{DBR} through thermo-optic effect by applying voltage to the heater. The maximum temperature change of the waveguide is $\approx 250 \text{ }^\circ\text{C}$,^[14] and the thermo-optic coefficient of Si_3N_4 is $2.43 \times 10^{-5} \text{ K}^{-1}$, meaning that maximum tuning leads to a refractive index shift of $\approx 6.075 \times 10^{-3} \text{ K}^{-1}$ in the Si_3N_4 waveguide. Using this, the tuned DBR was simulated with Ansys Lumerical EME. **Figure 9** shows the non-tuned DBR reflectance and the maximally tuned DBR reflectance of the DBR

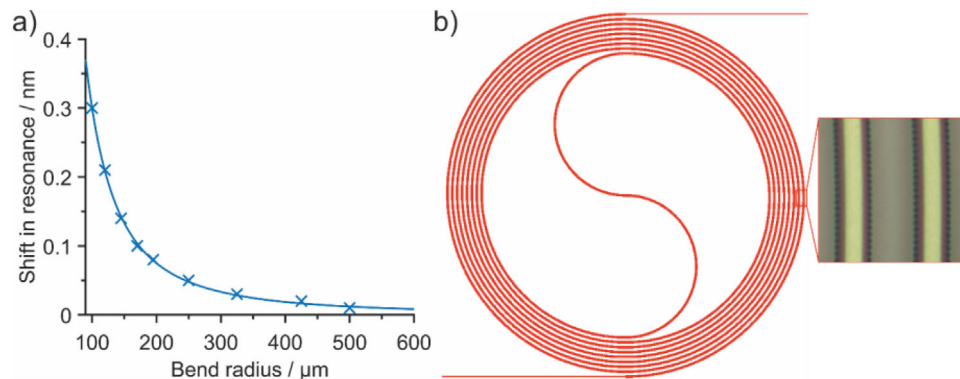


Figure 8. a) Simulated shift in DBR resonance as a function of Si_3N_4 waveguide bend radius, and b) a schematic of the spiral-shaped DBR, and a close-up microscope image showcasing the waveguide with circular posts positioned adjacent to it.

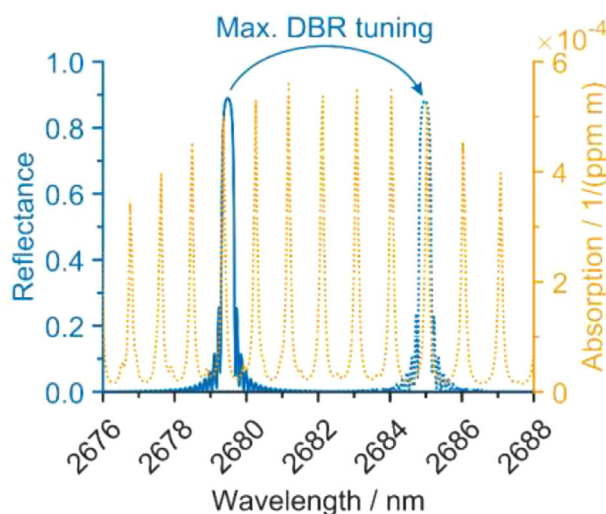


Figure 9. Simulated non-tuned DBR reflectance (blue line), maximally tuned DBR reflectance (blue dotted line), and the absorption of CO_2 ^[3] (orange dotted line) as a function of wavelength.

targeting CO_2 as a function of wavelength, together with CO_2 absorption. As is evident from the figure, the target absorption line at 2682.0 nm is located between the non-tuned and tuned DBR reflectance peaks. The same can be shown for the other absorption lines, meaning it is possible to tune the hybrid MWL to all the target absorption lines. In the hybrid MWL circuit an Archimedean spiral was placed at the output waveguide of the DBRs to suppress reflections.

4. Laser Performance

To form the hybrid MWL cavity shown in Figure 1, the RSOA was placed on a heatsink, which was stabilized to room temperature (23 °C). The output from the rear facet of the RSOA was coupled to a multimode (MM) fiber, which was coupled to a photodetector to measure the signal magnitude. The Si_3N_4 PIC was placed on a closed-loop piezo stage. The PIC was brought as close as possible to the RSOA with a differential adjuster, and a 2D piezo scan was performed to align the RSOA and PIC waveguides by maximizing the photodetector signal.^[14] The alignment accuracy achieved

was within <10 nm range, limited by the piezo controllers. The alignment gap between the RSOA and PIC was $\approx 1 \mu\text{m}$, set by the accuracy of the differential adjuster and the optical microscope resolution. Remarkably, no significant alignment drift was observed during the measurement.

The location of the RSOA gain maximum depends on the temperature of the active region, which can be adjusted by changing the duty cycle of the current injected to the RSOA. It was found that by utilizing a duty cycle of 50%, lasing is achieved at each DBR wavelength with mW-level operation. Thus, the hybrid MWL was operated in pulsed mode with a 100 kHz frequency and a 50% duty cycle.

Figure 10a shows the photodetector signal magnitude as a function of the power applied to the heater of one of the arms of the first MZI. The RSOA injection current was fixed at 500 mA. The figure has two maxima, and it can be confirmed from the spectrum of the laser that the first maximum corresponds to the case where light is transmitted to the output connected to the two DBRs targeting H_2O and CO_2 , and at the second maximum the light is transmitted to the output connected to the DBR targeting H_2S . **Figure 10b** shows the photodetector signal magnitude as a function of the power applied to the heater of one of the arms of the second MZI. Here the first MZI was tuned to the first maximum in **Figure 10a** to maximize transmission to the second MZI. The figure has two maxima, and it can be confirmed that at the first maximum, the light is coupled to the DBR targeting H_2O , and at the second maximum the light is coupled to the DBR targeting CO_2 , confirming the switching mechanism.

The current–light (IL) curve was measured for each DBR wavelength separately by switching the hybrid MWL between the different DBRs. **Figure 11** shows the IL curves when operating the hybrid MWL at the different DBR wavelengths. When operating at the H_2S DBR, the hybrid MWL has a threshold current of 185 mA, which is in line with the state-of-the-art Si_3N_4 -GaSb tunable laser demonstrated before, exhibiting similar threshold current.^[14] At the H_2S band laser reaches a peak average power of 5 mW at 410 mA. When operating the hybrid MWL at the CO_2 DBR, it shows a threshold current of 200 mA, and reaches a peak average power of 3.3 mW at 495 mA. Finally, when operating at the H_2O DBR, the hybrid MWL displays a threshold current of 210 mA, reaching a peak average power of 2.8 mW at 480 mA. The slightly higher threshold and lower output power

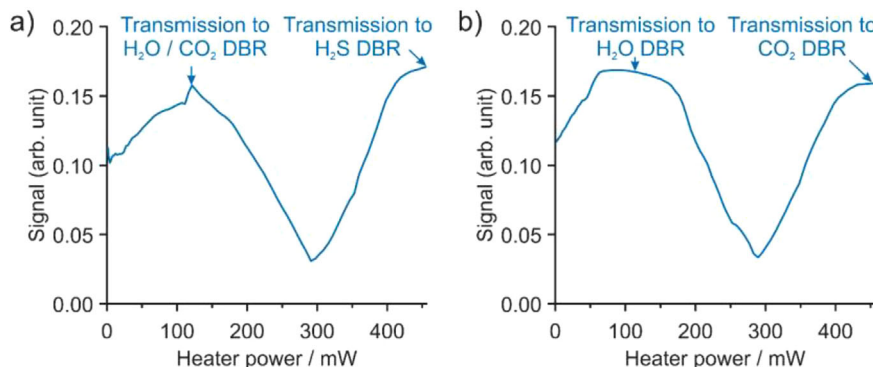


Figure 10. Photodetector signal as a function of power applied to a) the first MZI, and b) the second MZI.

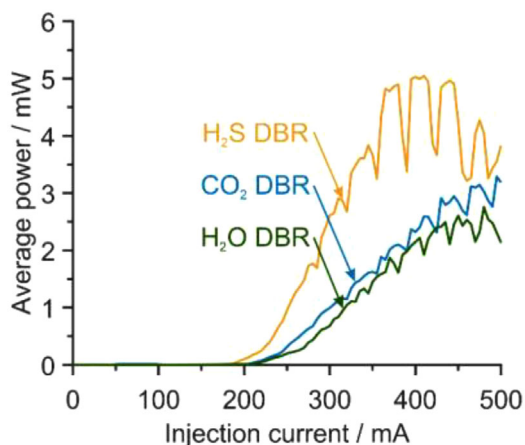


Figure 11. Average output power as a function of injection current when operating the hybrid MWL at the different DBR wavelengths.

when operating at the CO_2 and H_2O wavelengths can be partly explained by higher losses, due to the light having to pass through two MZIs, whereas when operating at the H_2S DBR, the light passes through only one MZI. The gain and threshold of the hybrid MWL are also affected by the gain of the RSOA, which is likely higher near the wavelength of the H_2S DBR than the wavelengths of the other two DBRs.

The output spectrum of the hybrid MWL for operation at each DBR was measured using a Fourier transform infrared (FTIR) spectrometer. A constant injection current of 400 mA was injected to the RSOA. **Figure 12a** shows the measurement result. The operation wavelengths for the CO_2 DBR, the H_2S DBR, and the H_2O DBR are 2670.42, 2629.12, and 2594.27 nm, respectively. Compared to the simulated values there is a shift of 9.06, 7.98, and 8.8 nm toward lower wavelength, respectively. Comparing DBR wavelengths between seven different PICs manufactured in the same MPW run, there is a standard deviation of roughly ≈ 1.0 nm in the resonance wavelength among the different PICs. This deviation is likely attributed to two main factors: inaccuracies in the available Si_3N_4 refractive index data used for simulation, or the systematic geometrical errors in DBR thickness and lateral dimensions. However, it is noteworthy that the observed wavelength variation falls within an acceptable range, as the DBRs exhibit a maximum wavelength tunability of ≈ 5 nm (Figure 9).

To demonstrate the tunability of the DBRs, the laser was switched to the CO_2 DBR, and power was applied to the heater on top of the DBR to tune its resonance wavelength. **Figure 12b** shows the spectrum without heating and for 140 mW heating power. The emission wavelength is 2670.42 nm without heating, and 2670.72 nm with heating, corresponding to ≈ 0.30 nm wavelength tuning at this power level. Here the heater power was limited by the resistance of the DBR heater. With an optimized

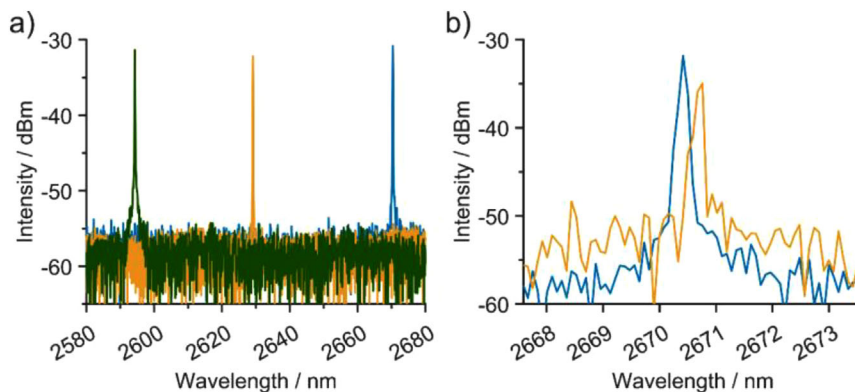


Figure 12. a) The spectrum of the hybrid MWL when operating at the CO_2 DBR (blue curve), the H_2S DBR (orange curve), and the H_2O DBR (green curve), and b) the spectrum of the hybrid MWL when operating at the CO_2 DBR without heating of the DBR (blue curve), and 140 mW applied to the DBR heater (orange curve).

heater design, we expect multi-nm tuning to be possible; this expectation is justified by the simulation result shown in Figure 9.

5. Conclusion

In conclusion, we have proposed and demonstrated a hybrid MWL that can be switched and tuned at 2670.42, 2629.12, and 2594.27 nm, targeting the absorption lines of CO₂, H₂S, and H₂O, respectively. Wavelength-selection was achieved with ≈12-cm-long spiral-shaped thermally tunable DBRs with Si₃N₄ posts placed next to the waveguide to achieve periodic index change. Switching was achieved with two cascaded thermally tunable MZIs, where the outputs are connected to the DBRs. Importantly, our method is easily scalable to accommodate additional wavelengths by increasing the number of MZIs and DBRs. This circuit configuration simplifies the tuning mechanism of a hybrid laser by having less control variables compared to conventional hybrid laser configurations, such as Vernier lasers. Furthermore, unlike previous MWL demonstrations that necessitate individual SOAs for each wavelength, the MWL configuration here only requires a single SOA. Low-loss (≈0.44 dB) and broadband MZIs were achieved by utilizing directional couplers with asymmetric waveguides in the coupling region to control the phase.

The hybrid MWL was operated with pulsed injection current at a frequency of 100 kHz and a duty cycle of 50%. Average output powers in the mW-level, and a threshold current near 200 mA were achieved for each operation wavelength, making such a light source attractive for sensing applications, such as the spectroscopic sensing of CO₂, H₂S, and H₂O. Based on our recent results for Vernier GaSb/Si₃N₄ hybrid lasers, CW-operation can be achieved by optimizing the wavelength for maximum gain of the RSOA.^[14] A shift in the DBR resonance wavelengths compared to the simulation was observed, caused most likely by the Si₃N₄ refractive index data available for simulation. The shift can be taken into account in future MPW runs to design PICs where the DBR resonances are closer to the target absorption lines.

With 140 mW heating power ≈0.3 nm of wavelength tuning was achieved. The tuning range of the DBR was limited by the high resistance of the DBR heater, which could be reduced significantly by designing a wider or thicker heater, or by decreasing the length of the DBR. Yet, in this last case, we should note a trade-off in terms of decreasing the DBR reflectance, which would have a negative effect on the laser performance. With an improved design, we expect multi-nm wavelength tuning to be achievable.

6. Experimental Section

Simulation and Numerical Methods: The directional couplers were simulated using Ansys Lumerical FDTD. Ports were placed at the input and output ports, and a finer mesh (0.1 μm) was used at the coupling region for improved simulation accuracy. The S-bend was optimized to achieve low insertion loss. In the conventional 50:50 DC, the coupling length was varied to achieve a 50:50 split ratio at a wavelength of 2.65 μm. For the 50:50 PC-DC, the taper length was optimized for low insertion loss, while the width of the waveguides in the asymmetric phase-control section was fixed. Subsequently, the symmetric coupler length and asymmetric phase-control section length were simultaneously swept and optimized to achieve a 50:50 split ratio over a broad wavelength band centered at 2.65 μm.

The distributed Bragg reflectors (DBRs) were simulated using Ansys Lumerical EME. To optimize the gap between the waveguide and DBR period, a single period of a straight DBR was simulated. The effect of the circular post was studied by dividing the waveguide region with the post into 51 cells with 10 modes. The DBR resonance wavelength was optimized by performing a series of simulations with different DBR periods and sweeping the wavelength to find the location of the DBR resonance wavelength. The reflectance and linewidth variation with DBR length were investigated by varying the number of DBR periods and sweeping the wavelength around the DBR resonance wavelength. The impact of wave-length bend radius on the DBR resonance location was examined by dividing the EME simulation region into 50 cells, adjusting the bend radius, orientation, and locations accordingly. The wavelength was then swept around the straight DBR resonance to determine the shifted DBR resonance location.

Experimental Methods: The PL measurement of the epimaterial was conducted using a 980 nm CW laser with a power of 60 mW. The laser beam was focused on the sample, and the emitted light was collected with a lens and directed into a monochromator. The monochromator swept the wavelength from 2000 to 2900 nm. A VIGO PVI-4TE-4 photodetector placed at the monochromator's output slit detected the light. An SR540 optical chopper with a chopping frequency of 260 Hz was positioned between the monochromator and the photodetector, and the signal magnitude of the photodetector was measured using an SR810 Lock In Amplifier synchronized with the optical chopper's trigger signal.

For the laser measurements, the RSOA was mounted on an AlN submount on a temperature-controlled heatsink stabilized at 23 °C. The rear facet output of the RSOA was coupled to a Thorlabs ZrF4 multimode fiber, and the fiber output was connected to a VIGO PVI-4TE-4 photodetector. A SR540 optical chopper with a chopping frequency of 300 Hz was placed between the fiber and the photodetector. The signal magnitude of the photodetector was measured using an SR810 Lock In Amplifier synchronized with the optical chopper's trigger signal.

The hybrid laser cavity was created by placing the Si₃N₄ PIC on a custom vacuum holder, which was securely attached to a Thorlabs 3-Axis NanoMax closed-loop piezo stage. The piezo stage was precisely controlled using Thorlabs KPZ101 Piezo Controllers and KSG101 Strain Gauge Readers. The coupling gap between the RSOA and PIC was manually adjusted using differential adjusters, while the y and z positions were optimized by performing a 2D raster scan utilizing the piezo controllers. The position yielding the maximum signal, as detected by the lock-in amplifier, was determined as the optimal position.

Power calibration was conducted by measuring the power of a reference device using an integrating sphere setup. The output of the device was coupled to a Newport 819C Gold Collimated Beam Integrating Sphere, and a VIGO PVI-4TE-4 photodetector was positioned at one of the sphere's outputs. Subsequently, the ASE output power from the rear facet of the RSOA was measured using the same setup. This measurement of the ASE output power enabled the calculation of the output power of the hybrid laser.

To tune the heaters on the PIC, the PIC was mounted on a glass substrate with metal pads. The heaters of the PIC were wire bonded to the pads, and a custom PCB with probes was connected to the metal pads. The PCB was linked to a Keithley 2604B Source Measure Unit to supply power to the heaters. The laser emission wavelength was switched between the different DBRs by scanning the MZI phase shifters and finding operation points where the laser wavelength matched the DBR resonances. The laser spectrum at each DBR resonance was recorded by coupling the fiber output to a Bristol Instruments 771B Laser Spectrum Analyzer. The DBR was tuned by applying a maximum power of 140 mW to the heater.

Acknowledgements

The research was funded by EU Business Finland projects RAPS1 (decision 1613/31/2018) and PICAP (decision 44761/31/2020) and Vaisala Oyj. This work is part of the Academy of Finland flagship program PREIN (decision 320168). S.-P. Ojanen would like to thank Vaisala Oyj for the funding of

the Ph.D. program. The authors wish to thank D.Sc. Heikki Virtanen for preparation of AR coatings.

Conflict of Interest

The authors declare no conflict of interest.

Data Availability Statement

The data that support the findings of this study are available from the corresponding author upon reasonable request.

Keywords

GaSb, hybrid lasers, laser diodes, mid-infrared lasers, multiwavelength lasers, photonic integrated circuits, silicon nitride photonics

Received: May 30, 2023

Revised: July 30, 2023

Published online:

- [1] M. Sieger, B. Mizaikoff, *Anal. Chem.* **2016**, *88*, 5562.
- [2] Z. Du, S. Zhang, J. Li, N. Gao, K. Tong, *Appl. Sci.* **2019**, *9*, 338.
- [3] I. E. Gordon, L. S. Rothman, C. Hill, R. V. Kochanov, Y. Tan, P. F. Bernath, M. Birk, V. Boudon, A. Campargue, K. V. Chance, B. J. Drouin, J.-M. Flaud, R. R. Gamache, J. T. Hodges, D. Jacquemart, V. I. Perevalov, A. Perrin, K. P. Shine, M.-A. H. Smith, J. Tennyson, G. C. Toon, H. Tran, V. G. Tyuterev, A. Barbe, A. G. Császár, V. M. Devi, T. Furtenbacher, J. J. Harrison, J.-M. Hartmann, A. Jolly, et al., *J Quant Spectrosc Radiat Transf* **2017**, *203*, 3.
- [4] A. K. Amerov, J. Chen, M. A. Arnold, *Appl. Spectrosc.* **2004**, *58*, 1195.
- [5] P. T. Lin, H. G. Lin, Z. Han, T. Jin, R. Millender, L. C. Kimerling, A. Agarwal, *Adv. Opt. Mater.* **2016**, *4*, 1755.
- [6] S. Dhall, B. R. Mehta, A. K. Tyagi, K. Sood, *Sens. Int.* **2021**, *2*, 100116.
- [7] S. S. Dhanabalan, S. Sriram, S. Walia, S. R. Avaniathan, M. F. Carrasco, M. Bhaskaran, *Adv. Photonics Res.* **2021**, *2*, 2000076.
- [8] K.-J. Boller, A. van Rees, Y. Fan, J. Mak, R. Lammerink, C. Franken, P. van der Slot, D. Marpaung, C. Fallnich, J. Epping, R. Oldenbeuving, D. Geskus, R. Dekker, I. Visscher, R. Grootjans, C. Roeloffzen, M. Hoekman, E. Klein, A. Leinse, R. Heideman, *Photonics* **2019**, *7*, 4.
- [9] Y. Guo, X. Li, M. Jin, L. Lu, J. Xie, J. Chen, L. Zhou, *APL Photonics* **2022**, *7*, 066101.
- [10] N. Zia, J. Viheriälä, R. Koskinen, A. Aho, S. Suomalainen, M. Guina, *Appl. Phys. Lett.* **2016**, *109*, 231102.
- [11] N. Zia, J. Viheriälä, E. Koivusalo, H. Virtanen, A. Aho, S. Suomalainen, M. Guina, *Appl. Phys. Lett.* **2018**, *112*, 051106.
- [12] K. Vizbaras, M.-C. Amann, *Semicond. Sci. Technol.* **2012**, *27*, 032001.
- [13] N. Zia, S.-P. Ojanen, J. Viheriälä, E. Koivusalo, J. Hilska, H. Tuorila, M. Guina, *Opt. Lett.* **2023**, *48*, 1319.
- [14] S. Ojanen, J. Viheriälä, N. Zia, E. Koivusalo, J. Hilska, H. Tuorila, M. Guina, *Laser Photonics Rev.* **2023**, *17*, 2201028.
- [15] R. Wang, S. Sprengel, A. Vasiliev, G. Boehm, J. Van Campenhout, G. Lepage, P. Verheyen, R. Baets, M.-C. Amann, G. Roelkens, *Photonics Res.* **2018**, *6*, 858.
- [16] S.-P. Ojanen, J. Viheriälä, M. Cherchi, N. Zia, E. Koivusalo, P. Karioja, M. Guina, *Appl. Phys. Lett.* **2020**, *116*, 081105.
- [17] R. Wang, S. Sprengel, G. Boehm, R. Baets, M.-C. Amann, G. Roelkens, *Optica* **2017**, *4*, 972.
- [18] G. Kurczveil, M. J. Heck, J. D. Peters, J. M. Garcia, D. Spencer, J. E. Bowers, *IEEE J. Sel. Top. Quantum Electron.* **2011**, *17*, 1521.
- [19] M. Wormington, C. Panaccione, K. M. Matney, D. K. Bowen, *Philos. Trans. R. Soc. Lond. Ser. Math. Phys. Eng. Sci.* **1999**, *357*, 2827.
- [20] Z. Lu, H. Yun, Y. Wang, Z. Chen, F. Zhang, N. A. F. Jaeger, L. Chrostowski, *Opt. Express* **2015**, *23*, 3795.
- [21] K. Solehmainen, M. Kapulainen, M. Harjanne, T. Aalto, *IEEE Photonics Technol. Lett.* **2006**, *18*, 2287.
- [22] C. Xiang, W. Jin, J. Guo, J. D. Peters, M. J. Kennedy, J. Selvidge, P. A. Morton, J. E. Bowers, *Optica* **2020**, *7*, 20.